Materials Science & Engineering A 613 (2014) 37–47

Contents lists available at ScienceDirect

Materials Science & Engineering A

journal homepage: www.elsevier.com/locate/msea

Effect of microstructural parameters, microtexture and matrix strain on the Charpy impact properties of low carbon HSLA steel containing MnS inclusions

A. Ghosh [a], S. Sahoo [b], M. Ghosh [c], R.N. Ghosh [a], D. Chakrabarti [a,*]

[a] Department of Metallurgical and Materials Engineering, I.I.T., Kharagpur 721302, India
[b] Research and Development, Tata Steel, Jamshedpur 831001, India
[c] CSIR – National Metallurgical Laboratory, Jamshedpur 831007, India

ARTICLE INFO

Article history:
Received 7 March 2014
Received in revised form
23 June 2014
Accepted 24 June 2014
Available online 1 July 2014

Keywords:
Charpy impact test
Ductile–brittle transition temperature
Upper shelf energy
MnS inclusions
Low-angle boundary fraction
Dislocation density

ABSTRACT

Low-carbon micro-alloyed steel containing coarse MnS inclusions was subjected to different thermo-mechanical processing routes to evaluate the effect of microstructure on its Charpy impact properties over a range of temperatures. MnS inclusions were found to deteriorate the upper shelf energy (USE) of the steel but its effect on the impact transition temperature was not as detrimental as that due to the presence of TiN particles. MnS inclusions were responsible for the initiation of micro-voids; however, the propagation of the cracks from these depends on the effective grain size and the strength of the matrix. An increase in the density of dislocations and low-angle boundaries enhances the strength and the strain-hardening ability of the ferrite matrix. This helps in retarding the growth of micro-voids, thereby reducing USE and promoting cleavage crack propagation resulting in an increase in its impact transition temperature. Refinement of effective grain size, on the other hand, increases the crack propagation resistance and therefore, improves the low-temperature toughness of the steel. Finish rolling of the steel just above the A_{r3} temperature (austenite to ferrite transformation start temperature) or a simple normalizing treatment of the as-rolled plates at a low austenitization temperature is recommended from the point of view of higher impact toughness and lower impact transition temperature.

1. Introduction

Excellent combination of high strength and high impact toughness is an essential requirement for thick steel plates used for the fabrication or construction of pressure vessels, ship hulls, line-pipes and various other strategic defense applications. Precipitation strengthening due to the presence of a fine dispersion of micro-alloying elements can increase the strength, but it adversely affects the impact toughness of the steel unless there is an accompanying refinement of its microstructure [1,2]. Thermo-mechanical controlled rolling provides significant grain refinement in high-strength low-alloy steels (HSLA). This helps improve the strength and toughness simultaneously [3–6].

The presence of hard and brittle particles in steel, such as TiN, can act as the potential sites for the initiation of cleavage and thus adversely affecting the impact toughness of steel [2,7–11]. A combination of large ferrite grain size and coarse TiN particles can seriously hamper the toughness of steel [2,11]. In a recent study, a few of the present authors have investigated the effect of processing and microstructural parameters on the impact toughness of Ti containing microalloyed steel (0.06 wt% C, 0.05 wt% Ti) [11]. The relative effects of ferrite grain size and TiN particle size in controlling the cleavage fracture have been discussed [11]. A refinement in ferrite grain size below a critical size is necessary to counteract the detrimental effect of the presence of coarse TiN particles on impact toughness at sub-zero temperatures [11].

MnS is a common type of inclusion that forms during the solidification of liquid steel [12–15]. Subsequent hot-rolling of the cast slab elongates MnS inclusions along the rolling direction in the form of stringers [12–16]. It has been reported that the presence of large MnS inclusions at high volume fraction deteriorates the impact toughness of steel [12–18]. The size and the volume fraction of MnS can be reduced by lowering the amounts of Mn and S in the hot metal [1]. However, desulfurization treatment delays the production process significantly. This adds to the production cost, and hence, it is beyond the scope of small scale steel producers and steel foundries [14]. In spite of having low Mn and S levels, it may also be difficult to avoid the formation of coarse MnS inclusions due to the occurrence of segregation during casting. In addition low Mn means lower solid solution strengthening [15], which has to be compensated by the addition of other

* Corresponding author.

http://dx.doi.org/10.1016/j.msea.2014.06.091
0921-5093/

alloying elements, such as, Ti and Cr into the steel. TiS and $Ti_4C_2S_2$ (titanium carbo-sulfide) inclusions are harder, less deformable and are more resistant to void nucleation than MnS [14,19]. However, Ti addition in steel increases the risk of TiN formation, which can cause premature brittle fracture [1,2,7–11]. On the other hand, CrS is more prone to void nucleation than MnS and hence, cannot be beneficial from the point of view of impact toughness [20].

Therefore, in spite of the presence of MnS inclusions the processing and microstructural parameters need to be adjusted carefully so that the impact toughness of the steel can be increased and impact transition temperature can be lowered. That sets the objective of the present study.

2. Experimental details

A 40 kg melt was prepared in an air-induction furnace. The composition of the heat is given in Table 1.

Table 1
Chemical composition of the investigated steel (wt%).

C	Si	Mn	S	P	Nb	V	N
0.08	0.30	1.20	0.03	0.02	0.05	0.08	0.007

The cast ingot (100 mm thick) was soaked at 1200 °C for half an hour and rolled in a laboratory rolling mill down to 15 mm thickness plates, following three different rolling schedules with finish rolling temperatures (FRT) of 820 °C (Sample code: FRT820), 730 °C (Sample code: FRT730) and 650 °C (Sample code: FRT650). The total rolling reduction remained constant (85%) in all the rolled plates. Samples taken from FRT730 plate were subjected to two different normalizing heat treatments using austenitization temperatures of 1150 °C (HT1150) and 940 °C (HT940) for 60 min and 5 min soaking time, respectively, before air cooling.

The cross-sections of the rolled and normalized samples were polished down to a 0.25 μm Al_2O_3 finish (aqueous solution) and etched in 2% nital. Microstructures and inclusions were studied by a Leica DM600M model optical microscope (fitted with Leica M.W. and Leica L.A.S. image analysis software) and a Zeiss EVO 60 model scanning electron microscope (SEM). The ferrite grain size was measured in terms of equivalent circle diameter (ECD) [22] based on the determination of grain area (image analysis) of more than 500 grains from each sample. The length of the elongated MnS inclusions was measured. It has been considered as the measure of its dimension or size. Electron backscattered diffraction analysis, EBSD, was carried out using an HKL Channel 5 system from Oxford Instruments, UK, attached to a Zeiss® EVO 60 SEM operated at a step-size of 0.3 μm to characterize the orientations of the ferrite

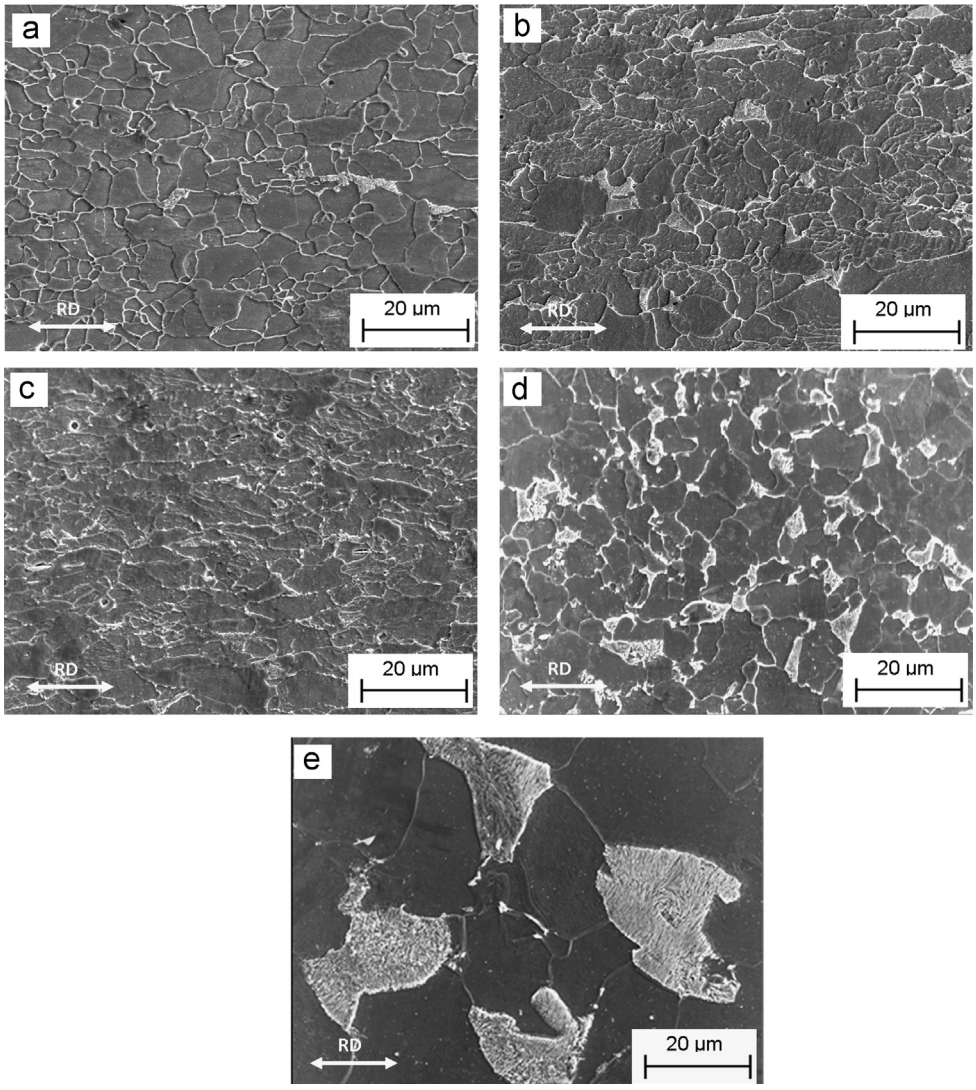

Fig. 1. SEM micrographs of the investigated samples: (a) FRT820, (b) FRT730, (c) FRT650, (d) HT940 and (e) HT1150. Rolling direction (RD) is indicated in all the images.

grains. Thin foils were prepared from the quarter-thickness locations of the rolled plates and were examined under a JEOL ZEM-2100 transmission electron microscope (TEM) to study the dislocation structure.

Tensile specimens were prepared from the samples developed by different processing conditions following ASTM E-8 standard [23] and tested with a cross-head velocity of 0.5 mm/min using an Instron® 8862 servo-electric test system (10 t) at room temperature (25 °C). An extensometer of 25 mm gage length was used for the accurate measurement of strain. Standard Charpy V-notch specimens were fabricated from the investigated steels and tested on an Instron® 400J impact machine (Model SI-1C3) attached with an Instron Dynatup Impulse data acquisition system, following ASTM E-23 standard [24], at various temperatures in the range from −196 °C to +60 °C. The sample temperature was maintained within ±2 °C using a medium of methanol and liquid nitrogen. A detailed fractographic study was carried out on the broken Charpy impact specimens. Macro-hardness was measured at 20 kg load using a LV-700 model LECO® Vickers tester and the average of five readings is considered to be a measure of its hardness. Nano-indentation studies have also been carried out using a Hysitron® TI050 Tribo Indenter at 2 mN load and 2 s dwell time. Nano-indentation readings were carefully taken from the center of the ferrite grains away from the grain boundaries.

3. Results and discussion

3.1. Characterization of microstructure and inclusions

Scanning electron micrographs of the investigated samples show the presence of ferrite and pearlite (Fig. 1) with the pearlite fractions varying within a close range of values (14–16%) (Table 2). The A_{r3} and A_{r1} temperatures predicted from the JMatPro® software for the investigated steel are 784 °C and 690 °C, respectively. The finish rolling temperatures (FRT) of FRT820, FRT730 and FRT650 samples, therefore, are within the austenite single-phase region, austenite–ferrite inter-critical region and ferrite–pearlite region, respectively. The true strain applied below A_{r3} temperature was 0.43 for FRT730 and 0.93 for FRT650 samples. Finish rolling above A_{r3} produced strain-free equiaxed ferrite grains in FRT820 sample (Fig. 1a) whilst, finish rolling below A_{r3} resulted in the formation of deformed ferrite grains in FRT730 and FRT650 samples (Fig. 1b and c). Pearlite colonies were also deformed and fragmented in FRT650 sample as the FRT was even below A_{r1} (Fig. 1c). The data given in Table 2 shows that the average ferrite grain size, as measured from the SEM micrographs, decreases with decreasing FRT. Strain-free and equiaxed ferrite grains formed even after the normalizing treatment, with the average ferrite grain size increased significantly with the increase in normalizing temperature (Table 2).

The EBSD band contrast images of the investigated samples are presented in Fig. 2. The thin lines in Fig. 2 represent the low-angle boundaries (2–15° misorientation angle) and the thick lines represent the high-angle boundaries (> 15° misorientation angle). The cumulative distribution of the grain boundary misorientaion angles in Fig. 3 shows that the fraction of low-angle boundaries increases with decreasing FRT (Table 2). Due to its high stacking fault energy deformed ferrite grains were in the recovered state, thereby increasing the density and fraction of low-angle 'sub-boundaries' in FRT730 and FR650 samples (Fig. 2b and c). In

Table 2
Microstuctural parameters, low-angle boundary fractions and the effective grain size of the investigated samples.

Sample code	Pearlite fraction (%)	Average ferrite grain size, ECD (μm)	LAB fraction (%)	Effective grain size (μm)
FRT820	14.3	9.6 ± 3.3	11.9	12.4
FRT730	15.7	8.2 ± 3.0	55.9	19.5
FRT650	16.6	5.9 ± 2.6	65.6	26.2
FRT940	15.8	9.7 ± 3.6	6.3	10.5
HT1150	14.1	40.7 ± 7.9	2	41.1

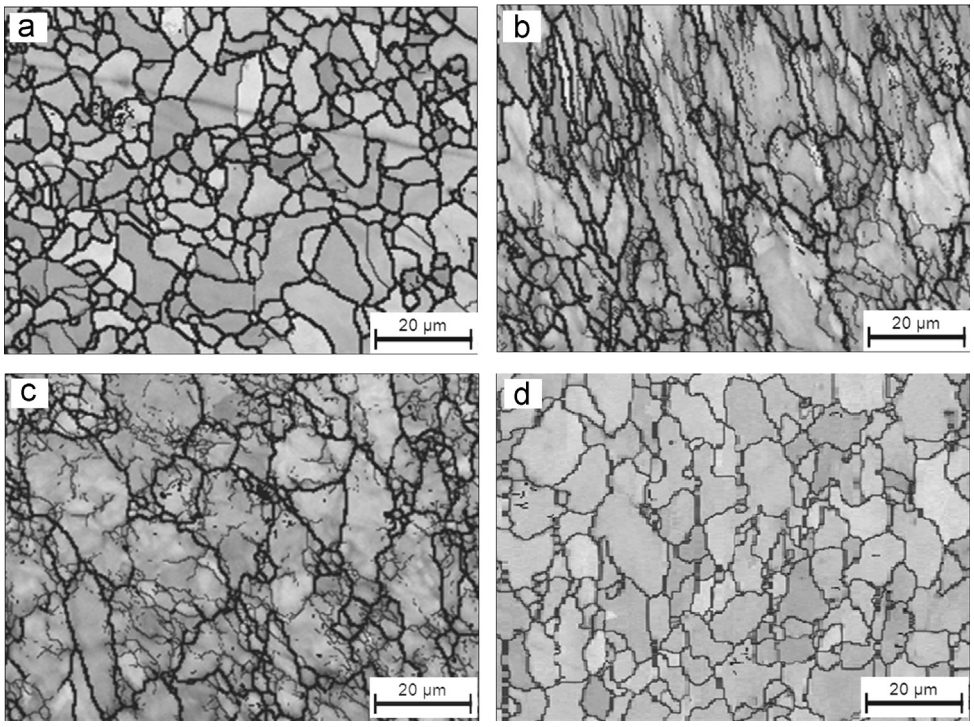

Fig. 2. Band contrast images of the investigated samples as obtained from the EBSD analysis: (a) FRT820, (b) FRT730, (c) FRT650, and (d) HT940.

comparison to the as-rolled samples, the low-angle boundary fraction in normalized samples appears to be significantly lower and it is found to decrease as normalizing temperature increases (Fig. 2d and Table 2). The low-angle boundaries are known to be not as effective as the high-angle boundaries in retarding the cleavage crack propagation [25–27]. The 'effective grain size' measured from the EBSD analysis considering only the high-angle boundaries (using 15° as the misorientation threshold) is listed in Table 2. It is found to be the lowest for HT940 and the highest for HT1150 (Table 2).

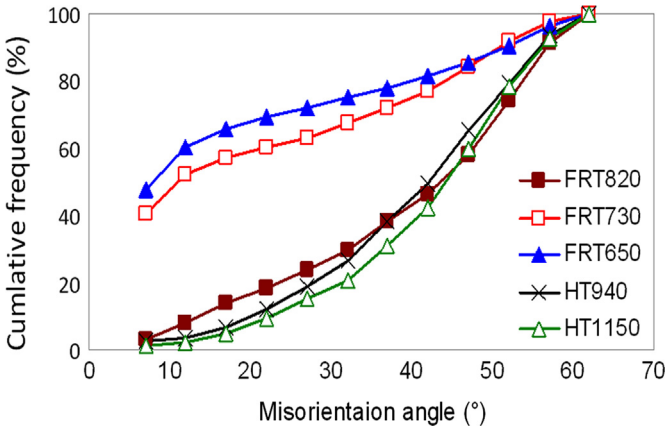

Fig. 3. Cumulative misorientation angle distribution of the investigated samples as obtained from the EBSD analysis.

Transmission electron micrographs of a set of samples that have gone through different processing routes are shown in Fig. 4a–d. The ferrite matrix in FRT820 sample was relatively strain-free having low dislocation density (Fig. 4a) whilst, dislocation cells and substructures were present in the ferrite matrix in FRT730 and FRT650 samples (Fig. 4b and c). The order of magnitude of dislocation density was found to be much higher in FRT650 ($\sim 10^{14}/m^2$) and FRT730 ($\sim 10^{13}/m^2$) samples, than that in FRT820 sample ($\sim 10^{9}/m^2$). Normalizing treatment was found to have significantly reduced the dislocation density down to $\sim 10^{8}$ to $10^{9}/m^2$ (Fig. 4d). The dislocation density has also been estimated using a different approach based on the EBSD analysis. The detailed methodology for measurement of dislocation density from EBSD analysis has been explained in a very recent work by Iza-Mendia et al. [28]. The estimated value of dislocation density from EBSD analysis matches well ($\pm$10% deviation) with the dislocation density measured from TEM analysis.

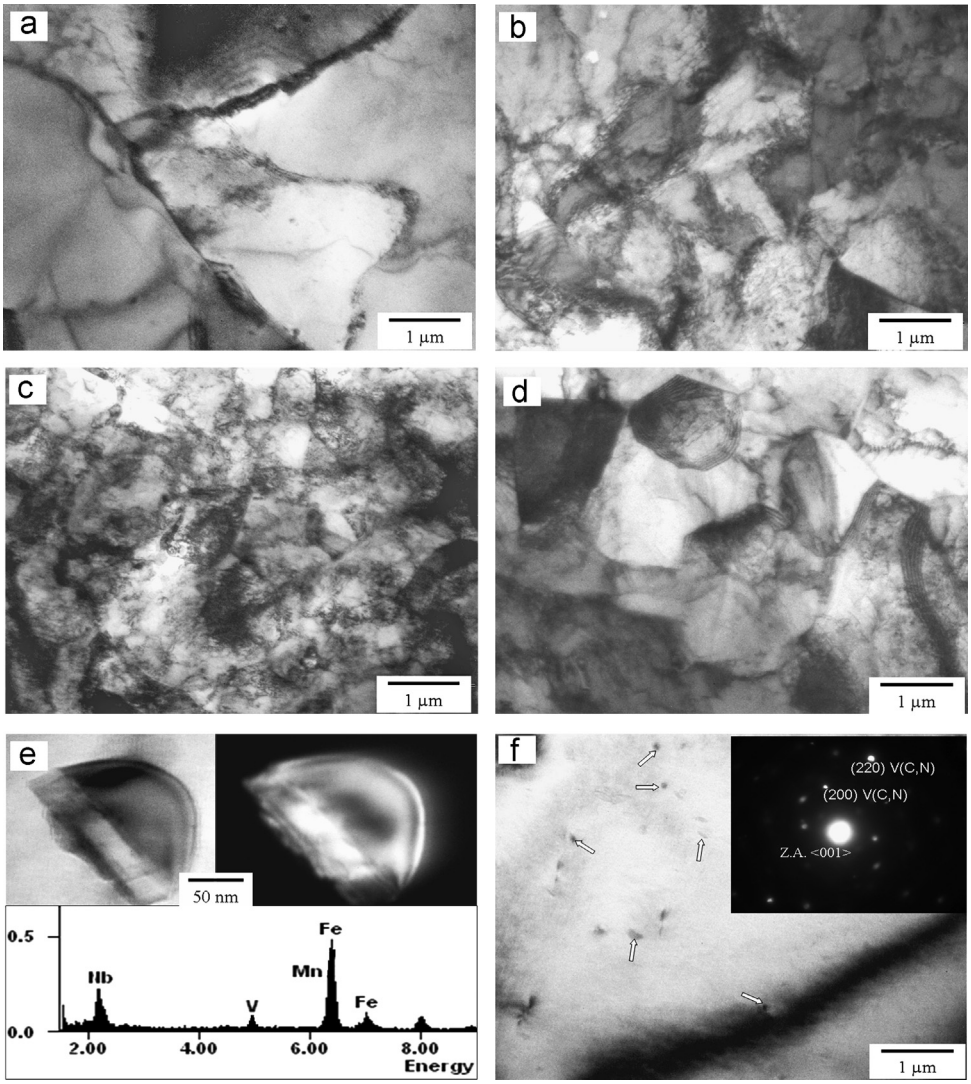

Fig. 4. Transmission electron micrographs of (a) FRT820, (b) FRT730, (c) FRT650 and (d) HT940 samples; (e) bright field and dark field TEM images of (Nb,V)(C, N) precipitate with the corresponding EDS analysis and (f) distribution of fine V(C,N) precipitates (arrowed) in the ferrite matrix with the corresponding SADP analysis.

The presence of fine Nb(C,N), V(C,N) and complex (Nb,V)(C,N) precipitates (10–100 nm) were also confirmed by Energy Dispersive Spectroscopy (EDS) (Fig. 4e), and Selected Area Diffraction Pattern analysis (SADP) (Fig. 4f) in all the samples. The morphology and distribution of the microalloy precipitate have been found to be similar in all the investigated samples.

Both Al_2O_3 and MnS inclusions were found to be present in all the samples, bulk of these were found to be made of MnS (~95% of all inclusions). MnS inclusions were elongated along the rolling direction in the form of stringers and the particle/matrix interface was often found to have separated (Fig. 5), possibly due to its low interfacial strength [29,30]. The volume fraction, size, aspect ratio and the inter-particle spacing of the inclusions in the as-rolled samples are listed in Table 3. At lower FRT, the inclusions were found to have fragmented into smaller particles (Fig. 5c), which reduce their average size and inter-particle spacing (Table 3). Normalizing treatment of the rolled steel did not alter the shape, size and distribution of the MnS inclusions. Manshadi and Dippenaar [14] studied the effect of deformation temperature on the deformation behavior of MnS in steel. Both recovery and recrystallization of austenite are ineffective at lower deformation temperatures. The rapid strain hardening of the matrix increases the difference between the hardness of the matrix and the inclusions. Therefore strain partitioning occurs from the harder matrix towards the softer inclusions [14] which leads to the separation of interface between the matrix and the inclusion. Decrease in the rolling temperature may also reduce the deformability of the inclusions; therefore it gets fragmented into smaller particles. Following Thermo-Calc® software, MnS is predicted to have formed immediately after solidification (at ~1468 °C) accompanying the formation of austenite. After subsequent austenite to ferrite transformation the inclusions, which appeared at the prior-austenite grain boundaries, were found to be present within the ferrite grains [21].

3.2. Hardness and tensile testing of the investigated samples

FRT650 has the highest macro-hardness and nano-indentation readings amongst all the investigated samples, followed by FRT730 sample (Table 4). Normalized samples showed lower hardness values than those of the as-rolled samples (Table 4). The presence of dislocation sub-structure with high dislocation density must have contributed to the high hardness in FRT730 and FRT650 samples. Macro-hardness indents covered several ferrite grains in each sample and hence, it represented the bulk hardness of the samples, whilst, the hardness measured by nano-indentation represents the hardness of a specific ferrite grain excluding the contribution from the ferrite grain boundaries. The tensile stress–strain curves of the samples are given in Fig. 6 and the tensile properties are listed in Table 4. In the investigated samples yield point phenomena have been observed and the lower yield point has been considered as the yield stress of the sample. Strength of the as-rolled samples increased with decreasing FRT. It has a direct correlation with the increase in applied strain below A_{r3} temperature. The increase in strength is however, accompanied by a

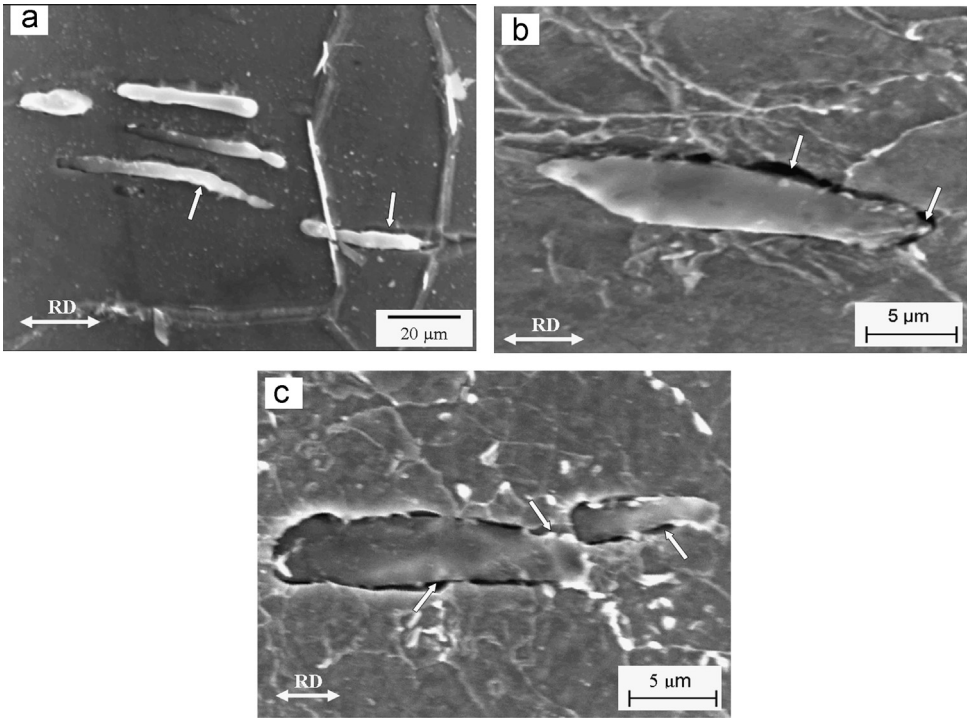

Fig. 5. (a and b) MnS inclusions elongated along the rolling direction (RD) in the ferrite matrix and (c) an example of a fragmented MnS inclusion. Arrows indicate decohesion of MnS inclusions from the ferrite matrix.

Table 3
Characterization of MnS inclusions in the as-rolled samples.

Sample code	Volume fraction (%)	Length (μm)	Thickness (μm)	Aspect ratio	Inter-particle spacing (μm)
FRT820	0.09	17.9 ± 2.4	1.8 ± 0.1	9.9 ± 2.3	50.2 ± 3.8
FRT730		13.7 ± 2.1	1.9 ± 0.1	7.2 ± 2.2	50.4 ± 4.6
FRT650		10.6 ± 1.6	1.7 ± 0.2	6.2 ± 1.3	39.9 ± 2.4

Table 4
Hardness and tensile properties of the investigated samples.

Sample	Macro-hardness (VHN)	Nanohardness (GPa)	Yields stress (MPa)	UTS (MPa)	Uniform elongation (%)	Area under the curve (J/m^3) × 10^3	n
FRT820	160	3.8	409	476	12.1	97.4	0.15
FRT730	188	4.7	509	572	8.4	78.6	0.11
FRT650	203	5.5	533	573	8.0	84.1	0.10
HT940	151	3.7	409	506	14.0	97.7	0.17
HT1150	132	3.6	258	415	17.5	85.9	0.20

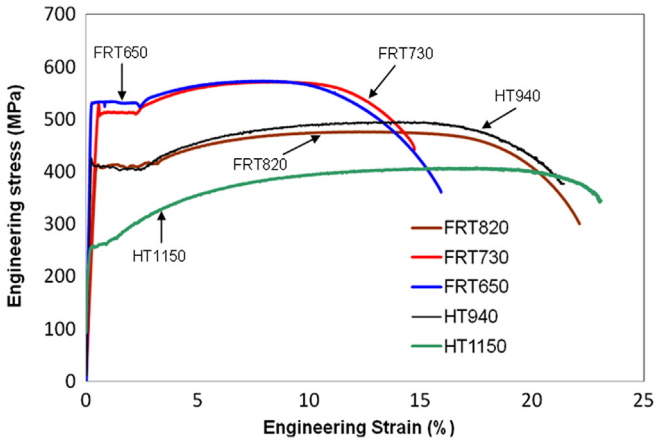

Fig. 6. Engineering stress–strain curves obtained from the tension tests on the investigated samples.

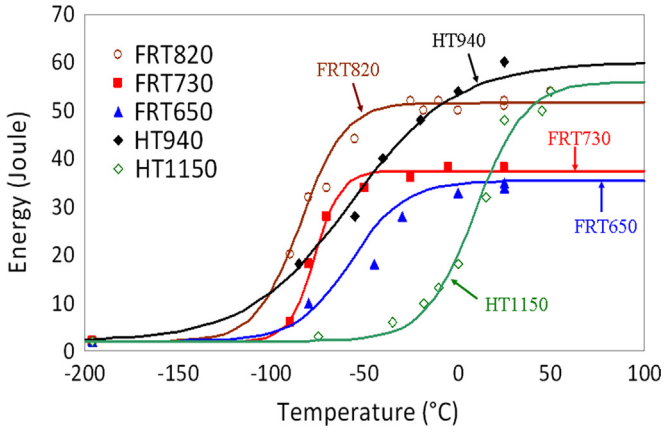

Fig. 7. Impact transition curves obtained from the Charpy impact test on the investigated samples.

corresponding decrease in uniform elongation and its strain-hardening exponent (n) (Table 4). High dislocation density and restricted dislocation activity resulted in high strength, but poor uniform elongation and low strain-hardening exponent in FRT730 and FRT650 samples (Table 4). On the other hand, highest strain-hardening exponent and uniform elongation in HT1150 sample (Table 4) can be attributed to the presence of strain-free ferrite matrix with coarse ferrite grain size. The tensile toughness, measured form the area under the stress–strain curve, was high in FRT820 and FRT940 samples, whilst, FRT730 samples showed the worst value (Table 4). Hence, considering the combination of strength, ductility, strain-hardening exponent and tensile toughness, FRT820 and HT940 samples were found to be superior in comparison to all other samples (Table 4).

3.3. *Charpy impact testing to determine the impact transition curves*

The Charpy impact transition curves (Fig. 7) were drawn within the scattered data points of Charpy impact energy vs. temperature plot by fitting a 'tanh' function, following the procedure given in [31]. The upper shelf energy (USE) and the ductile to brittle transition temperature (DBTT) were determined from the impact transition curves. These are listed in Table 5. The DBTT has been considered as the temperature halfway between the upper shelf energy and the lower shelf energy. The general yield load (P_{GY}) and the maximum load (P_{max}) were determined from the load vs. time traces obtained from the instrumented impact data following the established method given in [32]. Considering the variation in P_{GY} and P_{max} with respect to the test temperature, the cleavage fracture stress (σ_f) and the general yield temperature (T_{GY}) have been determined using the steps given in [32] (Table 5). T_{GY} is regarded as the impact transition temperature, where cleavage fracture coincides with the general yielding.

The range of USE of the investigated samples (35–60 J) is lower than the USE values commonly reported in literature (> 150 J) for

Table 5
Charpy impact toughness parameters for the investigated samples measured from instrumented impact test.

Sample name	USE (J)	DBTT (°C)	T_{GY} (°C)	Cleavage fracture stress (MPa) (σ_f)	Crack initiation energy (J)	Crack propagation energy (J)	Facet size (μm)
FRT820	51.6	−84.3	−96	1394	13.4	36	10.3 ± 1.1
FRT730	37.5	−76.5	−62	1525	5.6	32	18.2 ± 2.1
FRT650	35.4	−57.4	−44	1447	6.6	26	21.0 ± 3.4
HT940	60.0	−56.9	−86	1459	19.2	37	9.2 ± 0.8
HT1150	56.0	9.3	−10	914	34.9	21	40.0 ± 3.8

low-carbon micro-alloyed steels containing lower sulfur levels (< 0.01 wt% S) than the present steel [12,26,33–35]. This indicates to the harmful effect of MnS inclusions on the USE of the steel. Due to the low interfacial strength, MnS inclusions get easily de-bonded from the ferrite matrix, developing large elongated voids (Fig. 8a). Fig. 8b and c shows the nucleation of voids from MnS and MnS–Al_2O_3 complex inclusions, on a transverse plane perpendicular to the fracture surface of a broken Charpy impact specimen. Coalescence of the adjacent voids can lead to the formation of small micro-cracks (Fig. 8b), which may subsequently propagate to cause complete failure. Amongst the three different stages involved in ductile fracture, i.e. void nucleation, void growth and void coalescence, the growth stage consumes the maximum deformation energy. Therefore, USE increases as long as void growth takes place. When the void growth ceases, void coalescence begins, plastic instability sets in the ligament between the two adjacent voids, leading to the ligament necking [12,36]. McClintock [36,37] suggested that such plastic instabilities develop in the form of localized shear bands and the condition behind the formation of shear bands can be expressed by the

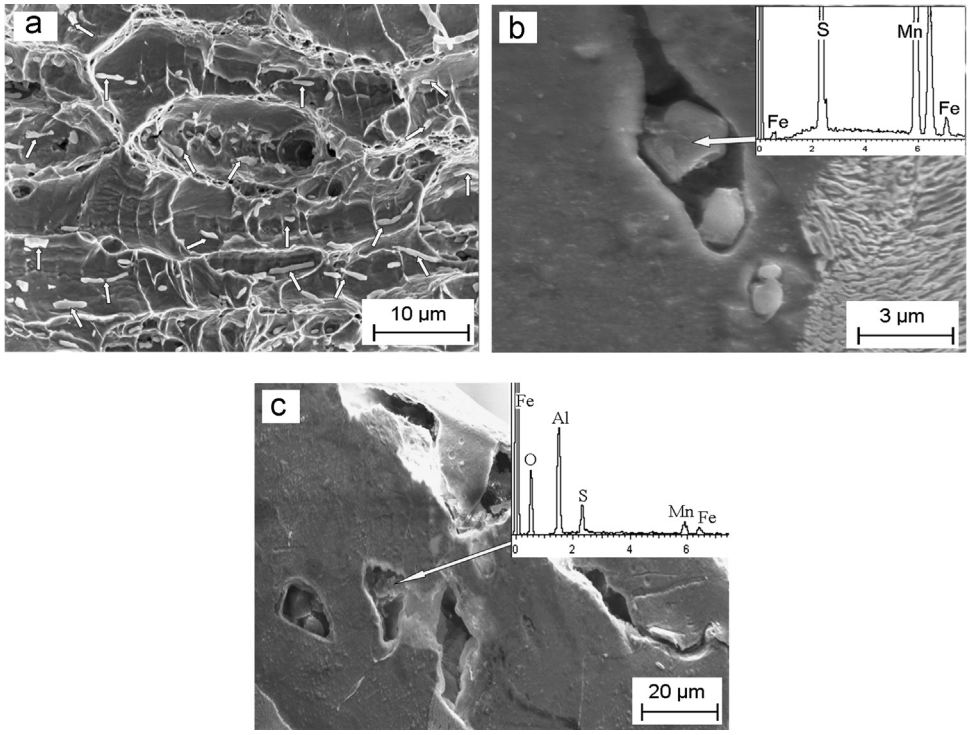

Fig. 8. (a) Presence of MnS inclusions (arrowed) inside the voids on the fracture surface of the Charpy impact tested sample tested at room temperature; SEM images on the transverse section just below the fracture surface of impact tested specimens showing the formation of cracks and voids from (b) the MnS inclusions and (c) MnS–Al_2O_3 complex inclusion.

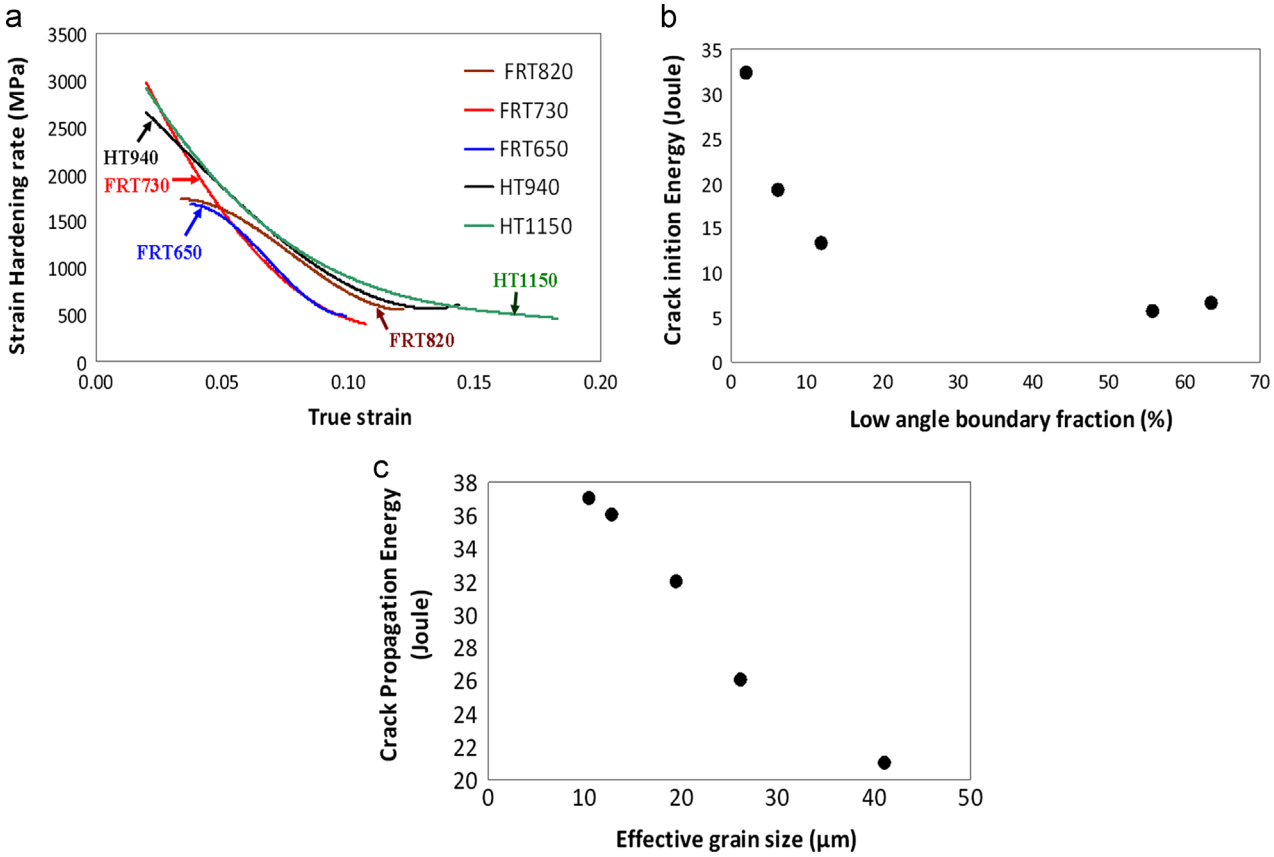

Fig. 9. (a) Variation of strain hardening rate with the true strain as obtained from the tensile test of the investigated samples; (b) variation of crack initiation energy with the low-angle boundary fraction and (c) the variation of crack propagation energy with the effective grain size of the investigated samples as obtained from the instrumented impact testing.

following equation [36,37]:

$$\frac{1}{\sigma}\left(\frac{d\sigma}{d\varepsilon}\right) < KF^2\left(\frac{v_f}{1-v_f}\right)\sqrt{\lambda^2+1} \quad (1)$$

where σ is the flow stress in terms of true stress, $(d\sigma/d\varepsilon)$ is the strain-hardening rate, v_f is the volume fraction, λ is the aspect ratio of the inclusions, K is a constant and F is the hole-growth factor. Eq. (1) indicates that the extent of void growth and hence, the impact energy absorption capacity of the steel not only depends on the inclusions parameters (i.e. volume fraction and the aspect ratio of MnS inclusions) but also on the strength and the strain-hardening ability of the ferrite matrix. Lower initial yield strength and higher strain hardening ability resist strain localization by the shear band formation. This promotes void growth and therefore, increases the capacity to absorb energy. The strain hardening rate $(d\sigma/d\varepsilon)$ derived from the tensile curves of the investigated samples is presented in Fig. 9a. Lower initial yield strength and higher strain-hardening rate, possibly contributes to higher USE in the normalized samples (HT940 and HT1150), as compared to those of as-rolled samples (Fig. 9a). On the other hand, high matrix strength and low strain-hardening rate result in low USE in FRT730 and FRT650 samples (35–37 J), whilst, FRT820 sample exhibits an intermediate value of USE (52 J) (Fig. 9a, Tables 4 and 5). The present results are in line with an earlier study [38], where USE of the steel rolled in the single-phase region above A_{r3} was found to be higher than that of the steel rolled below A_{r3}, i.e. within the two-phase region. High density of dislocations generated within the polygonal ferrite as a result of inter-critical deformation reduces the energy absorption capacity of ferrite [37].

Using the load-time data obtained from instrumented impact testing, the absorbed impact energy can be divided into two different components: (i) crack initiation energy is the energy absorbed till the maximum load is reached, and (ii) crack propagation energy is the energy absorbed beyond the maximum load till complete fracture [12]. In the present study, the crack initiation energy was found to have decreased with the increase in low-angle boundary fraction of the investigated samples (Fig. 9b). Low-angle boundaries increase the strength of the ferrite matrix [28,39], which hampers the extent of void growth and reduces the energy needed for crack initiation. A direct correlation between void growth and crack initiation energy was reported in an earlier study [40]. An effort has also been made to understand the effect of ferrite grain size on the energy needed for crack propagation. Average grain size appears to have little effect on the crack propagation energy, but Fig. 9c shows that the energy

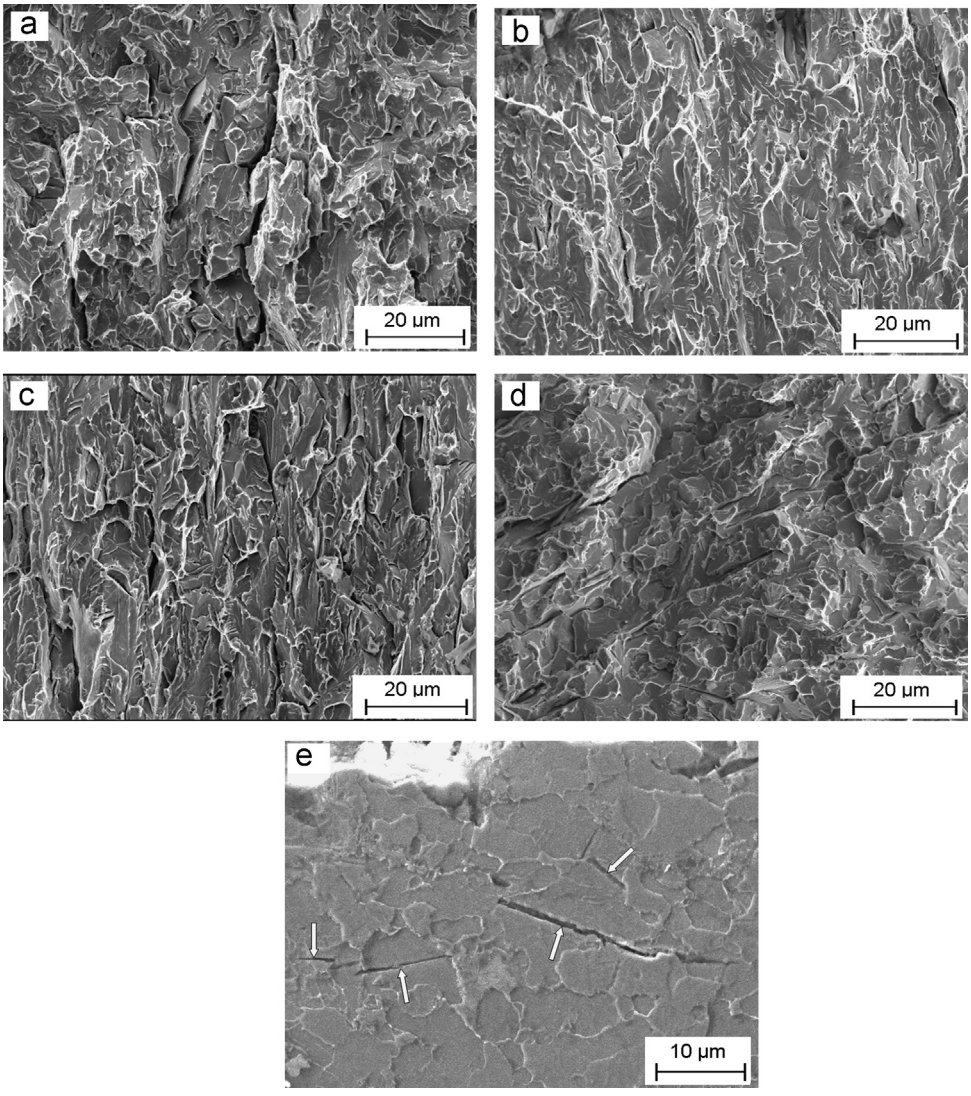

Fig. 10. SEM fractographs of the (a) FRT820, (b) FRT730, (c) FRT650, and (d) HT940 samples Charpy impact tested at −100 °C showing the cleavage facets; (e) presence of the secondary cleavage cracks just below the fracture surface in an impact tested FRT820 sample.

decreases with increasing effective grain size. Finer effective grain size, not only retards cleavage crack propagation at the lower shelf region, but also, resists ductile crack propagation at the upper shelf region.

The general yield load at certain temperature represents the load at which yielding occurs throughout the ligament of the sample. In the present study instrumented Charpy impact testing has been carried out over a range of temperature starting from room temperature (or above) down to −196 °C. With the decrease in the testing temperature the yield strength of the material increases which is expected to reduce the plastic zone size significantly. Therefore, below a certain temperature the yield stress of the material becomes so high that yielding throughout the ligament is not possible and the cleavage fracture occurs without the general yielding. Hence, from macro-scale fracture mechanics perspective the general yield temperature can be regarded as the impact transition temperature.

Amongst the investigated samples, FRT820 showed the lowest DBTT and HT1150 showed the highest DBTT (Fig. 7 and Table 5). The DBTT of FRT730 sample was also sufficiently low whereas those of FRT650 and HT940 samples were in the intermediate range (Table 5). The general yield temperature (T_{GY}) calculated from the load-time plot was much lower in HT940 sample. This indicates that the impact transition behavior of HT940 sample is superior to that of FRT650 sample. FRT820 showed the lowest T_{GY} and HT1150 sample showed the highest T_{GY} amongst all the samples (Table 5).

The range of DBTT of the present steel (+9 °C to −84 °C) was much lower than the range of values reported by Ghosh et al. in a recent study on low-carbon Ti-microalloyed steel (+30 °C to −33 °C) [11]. MnS inclusions are therefore, not as harmful as the TiN particles in terms of the impact transition temperature of low-carbon steels. The SEM fractographs of the impact tested samples (tested at −100 °C) in Fig. 10a–d show the presence of cleavage facets that follow the shape of the ferrite grains. The cleavage facets are elongated along the rolling direction in FRT730 and FRT650 samples, whilst, these are more equiaxed in FRT820 and HT940 samples (Fig. 10a–d). Sub-surface cracks are also preferentially oriented along the rolling direction in FRT730 and FRT650 samples, while, these are randomly oriented in FRT820 and HT940 samples (Fig. 10a–d). The average cleavage facet size measured from the fracture surfaces is the highest in HT1150 sample and the lowest in HT940 sample (Table 5). The facet sizes could not be correlated with the average ferrite grain size; however, the average facet size was found to be nearly the same as the effective ferrite grain size in all cases (Tables 2 and 5). This confirms the effectiveness of high-angle boundaries in resisting cleavage crack propagation as indicated by the earlier studies [25–27,34,41,42]. The presence of the secondary cleavage cracks covering the ferrite grains and the deflection or the complete stoppage of the cracks at the ferrite grain boundaries in FRT820 sample (Fig. 10e) indicates to the beneficial effect of small ferrite grain size and high-angle boundaries in lowering the impact transition temperature. The above statement can be further supported by the increase in T_{GY} temperature with the increase in effective grain size as presented in Fig. 11a.

An effort has been made to predict the general yield temperature from Harding's equation [43,44], which considers the dynamic yield stress (σ_{yd}) to be a function of test temperature (T °C) and ferrite grain size (D)

$$\sigma_{yd} = 350 - 2.5T + k_y D^{-1/2} \tag{2}$$

where the coefficient of grain boundary strengthening k_y=21 MPa mm$^{1/2}$ [45]. Apart from grain boundary strengthening ($\sigma_{gb} = k_y D^{-1/2}$) the contribution from other strengthening mechanisms,

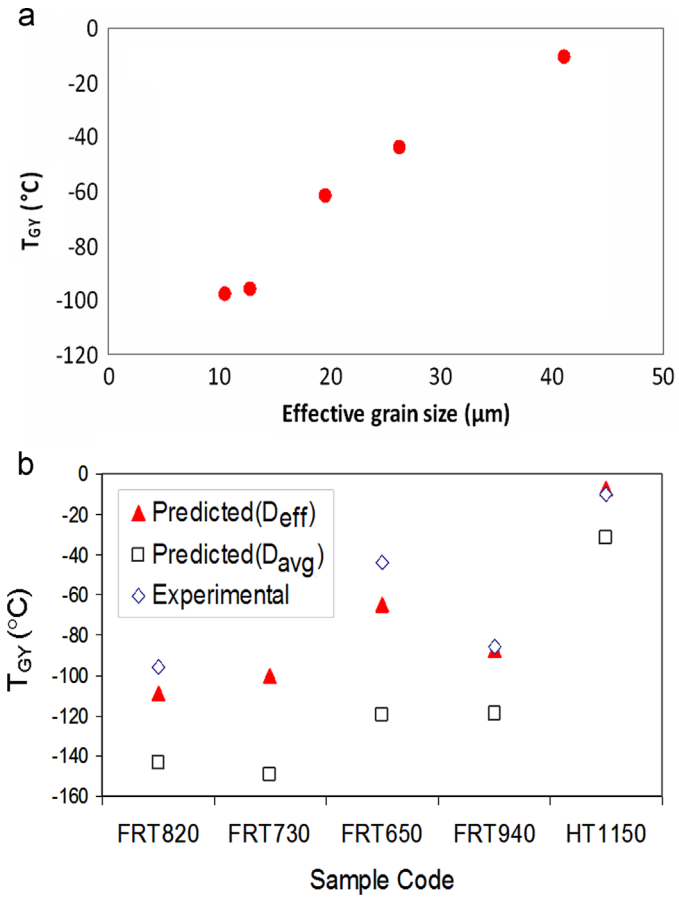

Fig. 11. (a) Variation of general yield temperature (T_{GY}) as the function of effective grain size and (b) prediction of general yield temperature for the investigated samples considering the average grain size (D_{avg}) and effective grain size (D_{eff}).

such as, precipitation strengthening (σ_p), dislocation strengthening (σ_d), and sub-grain strengthening (σ_{sg}) has not been considered in Harding's equation. The contribution of these to the dynamic yield strength might be described by the following equations [1,45,46]:

$$\sigma_p = \frac{0.3Gbv_f^{1/2}}{\bar{x}} \ln(\bar{x}/2b) \tag{3}$$

where v_f is the precipitate volume fraction, $\bar{x}$ is the average precipitate size and b is the Burger vector (0.248 nm).

$$\sigma_d = \alpha Gb\rho^{1/2} \tag{4}$$

where ρ is the dislocation density, G is the shear modulus (81 GPa) and α is a constant (0.5).

$$\sigma_{sg} = k_s l^m \tag{5}$$

where l is the average sub-grain size measured in terms of the intercept length, m is a constant (−0.5), and the coefficient of sub-grain boundary strengthening, $k_s \approx 2.1\sqrt{\theta}$, where θ is the average misorientation angle of the sub-grain boundaries.

At T_{GY}, σ_{yd} in Eq. (2) can be replaced by the cleavage fracture stress, σ_f, divided by the plastic constraint factor, K_{pcf}. K_{pcf} of the investigated samples has been calculated considering the crystallographic texture of the sample following the procedure reported in a recent study [47]. Using the calculated values of σ_f, T_{GY} can be predicted by the following equation:

$$T_{GY} = \frac{1}{2.5}\left[350 - \frac{\sigma_f}{K_{pcf}} + k_y D^{-1/2} + \sigma_p + \sigma_d + \sigma_{sg}\right] \tag{6}$$

The dislocation density, average size and fraction of the micro-alloy precipitates were determined from the TEM study and the

Table 6
Prediction of the general yield temperature of the investigated steel.

Sample name	σ_p (MPa)	σ_d (MPa)	σ_{sg} (MPa)	σ_t (MPa)	K_{pcf}	Experimental σ_{yd} at T_{GY} (MPa)	Predicted T_{GY} (°C)	Experimental T_{GY} (°C)
FRT820	56.7	3.1	27.7	87.5	1.95	714.9	−109	−96
FRT730	52.6	48.3	23.9	124.8	2.09	729.7	−100	−62
FRT650	50.6	61.1	29.7	141.4	2.2	657.7	−65	−44
HT940	51.4	3.1	25.4	79.9	2.23	654.3	−87	−86
HT1150	47.1	2.9	11.1	61.1	2.11	433.2	−8	−10

average sub-grain size and average misorientation angle across the low-angle sub-boundaries (misorientations between 2° and 15°) were obtained from the EBSD analysis.

The above micro-structural parameters have been used to estimate the contributions due to various strengthening mechanisms of interest for all the samples. These are listed in Table 6. The dynamic yield stress values measured at T_{GY} temperature is also included in Table 6. The prediction of T_{GY} following this approach has improved significantly when effective grain size is considered in the calculation in the place of the average ferrite grain size (Fig. 11b). A certain level of deviation is obvious; however, the trend in the variation in impact transition temperature is predicted reasonably well (Table 6 and Fig. 11b). The present calculation indicates that besides the effective grain size, it is also influenced by the strength of the ferrite matrix. High dislocation and sub-grain strengthening significantly increase the matrix strength of FRT730 and FRT650 samples. This results in higher impact transition temperatures (Table 6). However, HT1150 sample shows very high impact transition temperature, although its matrix strength is low. This is because of its high effective grain size.

Although, the initiation of cleavage fracture is known to depend on several factors, such as, the size of the non-metallic inclusions (i.e. TiN), volume fraction of pearlite colonies, interaction between the twins and the grain boundary carbide thickness [11,43,48], in blunt notch Charpy impact testing, cleavage fracture was reported to be controlled by the crack propagation across the ferrite grain boundary [49]. Hence, the T_{GY} temperature primarily depends on the ferrite grain structure and the matrix strength. DBTT, on the other hand, depends not only on the ability of the steel to resist cleavage fracture, but also on the magnitude of upper shelf energy [39]. The presence of MnS inclusions can influence USE either by initiation of micro-voids or by de-laminations along the fracture surface [50,51]. Future studies need to investigate these aspects separately in order to establish a quantitative relationship between the MnS inclusions and the USE and DBTT of the steel.

4. Conclusions

The following conclusions can be derived on the basis of the present study on micro-structural characterization, tensile and Charpy impact testing (over the fracture transition temperature) of rolled and normalized specimens of low-carbon micro-alloyed steel containing MnS inclusions.

(i) A decrease in the finish rolling temperature from 820 °C (FRT820) to 730 °C (FRT730) or to 650 °C (FRT650) increases the dislocation density of ferrite matrix, develops dislocation substructure and increases the fraction of low-angle boundaries.

(ii) Normalizing treatment at 940 °C (HT940) and 1150 °C (HT1150) develops strain free equiaxed ferrite grains with low dislocation density. The average and effective ferrite grain size increases significantly (from ~10 μm to ~41 μm) with an increase in normalizing temperature from 940 °C to 1150 °C.

(iii) The hardness and the strength of the as-rolled samples increase with the decrease in finish rolling temperature. The increase in strength is however, accompanied by a decrease in uniform elongation and strain-hardening ability. Normalizing treatment decreases the strength but improves the uniform elongation and strain-hardening ability of the steel.

(iv) The presence of MnS inclusions has a detrimental effect on the upper shelf energy (USE) of the steel. However, in terms of the impact transition temperature, MnS inclusions do not appear to be as harmful as the TiN particles.

(v) MnS inclusions are responsible for the initiation coarse micro-voids as a result of the separation of the inclusion–matrix interface. The subsequent growth of micro-voids and the propagation of the cleavage cracks depend on effective ferrite grain size and matrix strength.

(vi) Refinement of effective grain size is responsible for the improvement in low temperature impact toughness as the high-angle boundaries inhibit the propagation of cleavage micro-crack. Refinement of effective grain size also increases the ductile crack propagation energy at the upper shelf region of this steel.

(vii) The presence of higher dislocation density and finer sub-grains significantly increases the matrix strength of FRT730 and FRT650 samples. As a consequence both have higher impact transition temperatures. High matrix strength and low strain-hardening ability suppress the growth of micro-voids and thereby reduce USE. HT1150 sample showed high impact transition temperature, in spite of the low matrix strength, solely because of its high effective grain size.

(viii) Finish rolling just above the A_{r3} temperature (as in FRT820 sample) or normalizing treatment using low austenitization temperature (as in HT940 sample) can be recommended for achieving the best possible impact toughness, even in the presence of detrimental MnS inclusions.

Future studies are required to establish a quantitative relationship between the size and distribution of MnS inclusions and its USE and impact transition temperature.

References

[1] T. Gladman, The Physical Metallurgy of Microalloyed Steel, Book 615, The Institute of Materials, London, 1997.
[2] A. Echeverria, J.M. Rodrigue-Ibabe, Mater. Sci. Eng. A 346 (2003) 149–158.
[3] F. Siciliano, J.J. Jonas, Metall. Mater. Trans. A 31 (2000) 511–530.
[4] R. Song, D. Ponge, D. Raabe, J.G. Speer, D.K. Matlock, Mater. Sci. Eng. A 441 (2006) 1–17.
[5] H. Beladi, G.L. Kelly, P.D. Hodgson, Metall. Mater. Trans. A 38 (2007) 450–463.
[6] S. Patra, S. Roy, Vinod Lumar, A. Haldar, D. Chakrabarti, Metall. Mater. Trans. A 42 (2011) 2575–2590.
[7] M.A. Linaza, J.L. Romero, J.M. Rodriguez-Ibabe, J.J. Urcola, Scr. Mater. 32 (1995) 395–400.
[8] W. Yan, Y.Y. Shan, K. Yang, Metall. Mater. Trans. A 37 (2006) 2147–2158.
[9] D.P. Fairchild, D.G. Howden, W.A.T. Clark, Metall. Mater. Trans. A 31 (2000) 641–652.
[10] L.P. Zhang, C.L. Davis, M. Strangwood, Metall. Mater. Trans. A 32 (2001) 1147–1155.

[11] A. Ghosh, A. Ray, D. Chakrabarti, C.L. Davis, Mater. Sci. Eng. A 561 (2013) 126–135.
[12] D.K. Biswas, M. Venkatraman, C.S. Narendranath, U.K. Chatterjee, Metall. Trans. A 23 (1992) 1479–1492.
[13] Y.V. Murty, T.Z. Kattamis, R. Mehrabian, M.C. Flemings, Metall. Trans. A 8 (1977) 1275–1282.
[14] A.D. Manshadi, R.J. Dippenaar, Metall. Mater. Trans. A 41 (2010) 3291–3296.
[15] S. Maropoulos, N. Ridley, Mater. Sci. Eng. A 384 (2004) 64–69.
[16] Y. Tomita, Metall. Trans. A 19 (1988) 1555–1561.
[17] W.M. Garrison Jr., A.J. Wojcieszynski, Mater. Sci. Eng. A 505 (2009) 52–61.
[18] W.A. Spitzig, Metall. Trans. A 15 (1984) 1259–1264.
[19] J.L. Maloney, W.M. Garrison Jr., Scr. Mater. 23 (1989) 2097–2100.
[20] L.E. Iorio, W.M. Garrison Jr., Scr. Mater. 46 (2002) 863–868.
[21] G. Krauss, Metall. Mater. Trans. B 34 (2003) 781–792.
[22] D. Chakrabarti, C.L. Davis, M. Strangwood, Mater. Charact. 58 (2007) 423–438.
[23] ASTM E8/E8M-09, Standard Test Methods for Tension Testing of Metallic Materials, Annual Book of ASTM Standards, vol. 03.01, ASTM International, Pennsylvania, USA, 2005.
[24] ASTM E23-0.5, Standard Test Methods for Notched Bar Impact Testing of Metallic Materials, Annual Book of ASTM Standards, vol. 03.01, ASTM International, Pennsylvania, USA, 2005.
[25] M.C. Kim, Y.J. Oh, J.H. Hong, Scr. Mater. 43 (2000) 205–211.
[26] D. Bhattacharjee, C.L. Davis, Scr. Mater. 47 (2002) 825–830.
[27] S.J. Wu, C.L. Davis, J. Microsc. 213 (2004) 262–272.
[28] A. Iza-Mendia, I. Gutierrez, Mater. Sci. Eng. A 561 (2013) 40–51.
[29] S.B. Hosseini, C. Temmel, B. Karlsson, N.G. Ingesten, Metall. Mater. Trans. A 38 (2007) 982–989.
[30] I. Sobirov, O. Kolednik, Scr. Mater. 53 (2005) 1373–1378.
[31] Y. Sakai, K. Tamanoi, N. Ogura, Nucl. Eng. Des. 115 (1989) 31–39.
[32] W.L. Server, J. Test. Eval. 6 (1978) 29–34.
[33] A. Ray, S. Sivaprasad, D. Chakrabarti, Int. J. Fract. 173 (2012) 215–222.
[34] T. Hanamura, F.X. Yin, K. Nagai, ISIJ Int. 44 (2004) 610–617.
[35] B. Hwang, C.J. Lee, S. Kim, Metall. Mater. Trans. A 42 (9) (2011) 717–728.
[36] F.A. McClintock, Int. J. Fract. Mech. 40 (1968) 101–130.
[37] F.A. McClintock, Ductility, vol. 3, ASM, Metals Park, OH (1968) 255–277.
[38] B. Hwang, S. lee, Y.M. Kim, N.J. Kim, J.Y. Yoo, Metall. Mater. Trans. A 36 (9) (2005) 1793–1805.
[39] N. Hansen, Scr. Mater. 51 (2004) 801–806.
[40] Y.M. Shi, J.T. Barnby, A.S. Nadkarni, Eng. Fract. Mech. 39 (1991) 37–44.
[41] M.C. Zhao, T.Y. Zeng, J.L. Li, H. Xiaofang, Y.C. Zhao, A. Atrens, Mater. Sci. Eng. A 528 (2011) 2107–2114.
[42] B. Hwang, Y.G. Kim, S. Lee, Y.M. Kim, N.J. Kim, J.Y. Yoo, Metall. Mater. Trans. A 36 (2005) 2107–2114.
[43] N.J. Petch, Acta Metall. 34 (1986) 1387–1393.
[44] J. Harding, Acta Metall. 17 (1969) 949–958.
[45] J. Lu, O. Omotoso, J.B. Wiskel, D.G. Ivey, H. Henein, Metall. Mater. Trans. A 43 (2012) 3043–3061.
[46] J. Majta, J.G. Lenard, M. Pietrzyk, Mater. Sci. Eng. A 208 (1996) 249–259.
[47] A. Ghosh, S. Kundu, D. Chakrabarti, Scr. Mater. 81 (2014) 8–11.
[48] J.F. Knott, Fundamentals of Fracture Mechanics, Butterworths, London, 1973.
[49] J.H. Chen, G.Z. Wang, H. Ma, Metall. Mater. Trans. A 21 (1990) 321–330.
[50] B. Mintz, E. Maina, W.B. Morrison, Mater. Sci. Technol. 23 (2007) 347–354.
[51] R. Punch, M. Strangwood, C.L. davis, Metall. Mater. Trans. A 43 (2012) 4622–4632.